Available online at www.sciencedirect.com
ScienceDirect
Optics Communications 281 (2008) 880–887
OPTICS COMMUNICATIONS
www.elsevier.com/locate/optcom

An optical technique for remote focusing in microscopy

E.J. Botcherby, R. Juškaitis, M.J. Booth, T. Wilson *

University of Oxford, Department of Engineering Science, Parks Road, OX1 3PJ, UK

Received 9 August 2007; accepted 3 October 2007

Abstract

We describe the theory of a new method of optical refocusing that is particularly relevant for confocal and multiphoton microscopy systems. This method avoids the spherical aberration that is common to other optical refocusing systems. We show that aberration-free refocusing can be achieved over an axial scan range of 70 μm for a 1.4 NA objective lens. As refocusing is implemented remotely from the specimen, this method enables high axial scan speeds without mechanical interference between the objective lens and the specimen.

Keywords: Sectioning microscopy; High numerical aperture theory

1. Introduction

A common requirement in high-resolution optical microscopy is to obtain a three-dimensional representation of the object under investigation. This is typically achieved via an intermediate step using an optical sectioning technique, such as confocal microscopy [1], to eliminate the out-of-focus blur in order to obtain a clean in-focus image of a single plane within the sample. This process is repeated a number of times at different focal settings and gradually a full three-dimensional data set containing information about the whole object is gathered. This information can then be displayed and manipulated on a computer to reveal a wealth of information about the object structure.

In most practical implementations a single in-focus image can be acquired very quickly. However, the real bottleneck in three-dimensional data acquisition is the process of refocusing the microscope to successive image planes. High-resolution microscope objective lenses are designed to provide aberration-free images from a unique focal plane. There are fundamental optical reasons why it is not possible to achieve decent imaging at different image conjugates in high-aperture microscopy as opposed to, say, photographic cameras where such imaging is routine. Therefore the only viable solution in microscopy, up until now, has been to keep the imaging plane fixed and to change the distance between the object and imaging lens mechanically. Attempts have been made to improve the speed at which this can be done by using piezoelectric elements [2,3] however this speed is still limited by the fact that the imaging lenses and/or the specimen are relatively heavy. Apart from the speed limitations, these methods can also suffer from other disadvantages, which make imaging of delicate samples, such as live cell cultures, very difficult.

An alternative focusing method that does not involve mechanical movements near the specimen is clearly preferable. This would avoid specimen agitation and potentially permit axial scan speeds higher than those in existing microscopes. Attempts have also been made to do the refocusing remotely using vari-focus lenses [4], micro electromechanical mirrors [5] and acousto-optics modulators [6] but all suffer from aberrations introduced by the focusing elements. It has also been suggested that deformable mirrors could be used to correct the aberrations in conjunction with one of these focusing methods, but this introduces an extra unnecessary level of complexity to the system.

In this paper we will review, from a theoretical standpoint, the problems associated with refocusing in high

* Corresponding author.
E-mail address: tony.wilson@eng.ox.ac.uk (T. Wilson).

0030-4018/$ - see front matter © 2007 Elsevier B.V. All rights reserved.
doi:10.1016/j.optcom.2007.10.007

numerical aperture (NA) microscopy. We will then investigate an optical method [7], that circumvents many of these problems and enables refocusing to be carried out remotely without the introduction of systematic aberration and analyze the range of operation. Finally we characterize the system by measuring detection point spread functions (PSFs) experimentally to demonstrate the effectiveness of our approach.

2. Imaging in three-dimensions

In what follows we shall confine ourselves to the class of optical systems that are rotationally symmetric about the optic axis and so it is possible to restrict our analysis to the meridional plane without loss of generality. A concept that is useful when considering optical instruments is that of a *perfect imaging system*. Such a system is one that can form a stigmatic image of any point from a three-dimensional domain or equivalently forces all rays emanating from a single point in object space to re-converge at a single point in image space.

Such a system is shown in Fig. 1a where the object and image spaces are immersed in media of refractive indices n_1 and n_2 respectively. A single ray is shown emanating from the origin of object space with angle γ_1 along with the conjugate ray that it is mapped onto, which travels through the origin of image space with angle γ_2. We show how four point sources placed at different locations in the meridional plane are imaged by this system and further show explicitly how the rays converge for one of the points. The angular spectrum of rays that emerges in the region beyond the image space is therefore identical to that produced by the original object within the angular passband of the system.

The requirement of perfect three-dimensional imaging imposes quite a constraint on the design parameters of such a system and it has already been shown by Maxwell in 1858 [8] that the magnification M must necessarily be the same along all directions and have a magnitude of

$$|M| = \frac{n_1}{n_2}, \tag{1}$$

which for many situations is close to unity as n_1 and n_2 often have similar values. It can be shown [9] that this requirement also implies that all conjugate rays must propagate with the same angle with respect to the optic axis, i.e.:

$$\gamma_2 = \pm\gamma_1. \tag{2}$$

It can also be stated that any system that introduces a magnification different from Eq. (1) cannot be a perfect imaging system. Such is the case in microscopy, for instance, where systems are designed to grossly magnify the object under investigation and consequently there is a breakdown of perfect three-dimensional imaging. For cases where the object is of small linear dimensions, however, it is still possible to maintain perfect imaging for a subset of points in object space and there are two well known design conditions. These are the sine condition, which enables points in a plane, perpendicular to the optic axis, to be imaged perfectly, and the Herschel condition which allows points along the axis to be imaged perfectly [9]. It is often necessary to chose between these two conditions according to the application.

Most microscopes are designed according to the sine condition, however, and in Fig. 1b we show how such a system behaves when imaging the same array of point sources. Here we see that points lying in a unique plane, shown as a dashed line in object space, are imaged stigmatically in image space with a lateral magnification of M_1 whereas points displaced axially form non-stigmatic images. The paraxial rays still converge, however, with an axial magnification of $M_1^2 n_1/n_2$, whereas the rays traveling

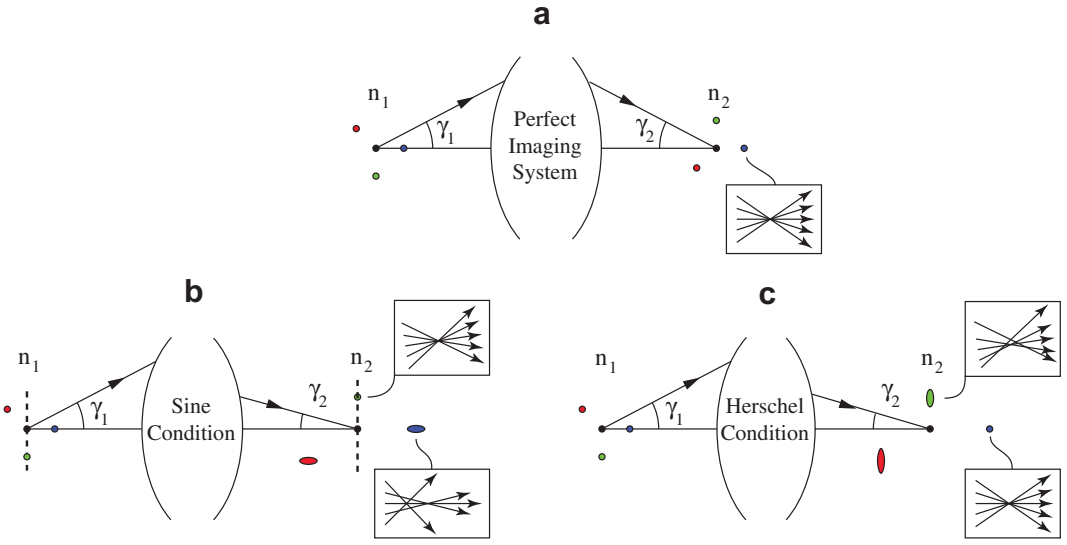

Fig. 1. Imaging four point sources in the meridional plane using (a) a perfect imaging system, (b) a system obeying the sine condition and (c) a system obeying the Herschel condition.

at higher angles tend to focus to points closer to the focal plane. This effect is commonly referred to as spherical aberration and gets progressively worse for larger axial displacements. The sine condition also imposes a different transformation between the conjugate rays, as shown, which is described by the following equation:

$$\sin\gamma_2 = \frac{n_1}{n_2}\frac{\sin\gamma_1}{M_1}. \tag{3}$$

From these considerations it is possible to see why commercial microscopes, operating under the sine condition refocus by changing the distance between the specimen and objective, as any attempt to detect images away from the optimal image plane will lead to a degradation by spherical aberration.

In Fig. 1c we show how a system obeying the Herschel condition behaves when imaging the array of point sources. In direct contrast with the sine condition, points lying along the optical axis are now imaged perfectly in the image space with an axial magnification of M_a whereas laterally displaced point are not. The transformation between conjugate rays in this case is given by:

$$\sin^2(\gamma_2/2) = \frac{n_1}{n_2}\frac{\sin^2(\gamma_1/2)}{M_a}. \tag{4}$$

For the specific case where a system is designed to obey the sine condition with a lateral magnification of $M_1 = n_1/n_2$ Eq. (3) reduces to Eq. (2) and perfect imaging then follows for the whole three-dimensional domain. In the same way, a system designed to obey the Herschel condition with an axial magnification of $M_a = n_1/n_2$ also permits perfect imaging with Eq. (4) once more reducing to Eq. (2).

3. The general pupil function

We now take a closer look at the specific geometry of a high NA microscope objective which can be modelled as a pair of principal surfaces that are spherical and planar in shape as shown in Fig. 2. A point source, placed at the origin of object space, emits a spherical wave which, upon crossing the principal sphere, is transformed into a plane wave in the pupil. A low NA tube lens (not shown) can then be used to focus this plane wave stigmatically to a point in image space. A point placed at some different location, $\mathbf{r} = (x, y, z)$, also emits a spherical wave but in this case different parts of the wavefront cross the principal sphere at

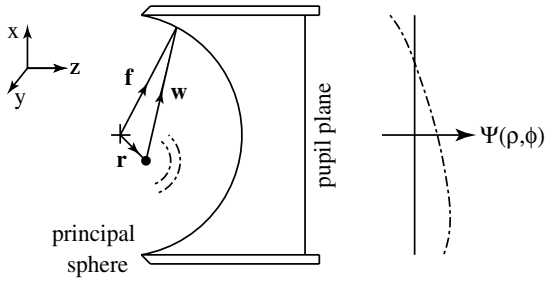

Fig. 2. A general microscope system.

different times producing a more complex phase profile in the pupil plane. We denote a general point on the principal surface with vector $\mathbf{f}$, which has a magnitude of f, and draw a second vector $\mathbf{w}$ from the point source to this same point. The relative path length difference between these rays is given by:

$$PD = |\mathbf{w}| - f = |\mathbf{f} - \mathbf{r}| - f = \{f^2 - 2\mathbf{f}\cdot\mathbf{r} + r^2\}^{1/2} - f, \tag{5}$$

where r is the magnitude of the source displacement. We can develop this further by writing each component of $\mathbf{f}$ in spherical polar form, $\mathbf{f} = f(\sin\theta\cos\phi, \sin\theta\sin\phi, \cos\theta)$:

$$PD = f\left\{1 - \frac{2}{f}(x\sin\theta\cos\phi + y\sin\theta\sin\phi + z\cos\theta) + \frac{r^2}{f^2}\right\}^{1/2} - f. \tag{6}$$

Expanding this to first order, assuming $r \ll f$, gives:

$$PD \approx -\frac{\mathbf{f}\cdot\mathbf{r}}{f} = -(x\sin\theta\cos\phi + y\sin\theta\sin\phi + z\cos\theta), \tag{7}$$

which, interestingly, does not depend on f. The phase profile in the pupil plane can be found by invoking the sine condition which maps rays between the principal surfaces whilst preserving their distance from the optic axis:

$$\sin\theta = \rho\sin\alpha. \tag{8}$$

In this expression α is the semi-aperture acceptance angle of the lens and ρ is the normalized pupil radius. Applying this transformation and multiplying the result by the vacuum wavenumber k leads to an expression for the phase profile in the pupil plane as function of the point source position:

$$\Psi(\rho,\phi;\mathbf{r}) \approx nk\sin\alpha\left\{x\rho\cos\phi + y\rho\sin\phi + z\sqrt{\frac{1}{\sin^2\alpha} - \rho^2}\right\}, \tag{9}$$

where a refractive index of n has been included to account for the case where the focal region is surrounded by an immersion medium and ϕ, which was previously the azimuthal angle in object space becomes the azimuthal angle in the pupil plane.

There are a number of conclusions that can be drawn from the form of this pupil function. First, it can be seen that lateral displacements of the point source produce plane waves in the pupil with an amount of tip ($\rho\cos\phi$) or tilt ($\rho\sin\phi$). These flat waveforms, which are a direct result of the sine condition, are then focussed stigmatically by the tube lens to laterally displaced points in image space. Second, we see that axial displacement leads to a curved phase profile which can be expanded in powers of ρ to give:

$$znk\sqrt{1 - \rho^2\sin^2\alpha} = znk\left\{1 - \frac{\rho^2\sin^2\alpha}{2} + \frac{\rho^4\sin^4\alpha}{8} + \cdots\right\}, \tag{10}$$

which may be thought of as the phase profile for high NA defocus. Focussing using the tube lens is accurately

described by the quadratic term, as it operates in the paraxial regime. Unfortunately the higher order terms which represent spherical aberrations cannot be focussed by the tube lens and consequently there is a breakdown of stigmatic imaging for these points.

If on the other hand the objective had been designed to satisfy the Herschel condition, to give perfect axial imaging, the mapping of Eq. (8) would be replaced by:

$$\sin(\theta/2) = \rho \sin(\alpha/2), \tag{11}$$

and the corresponding phase function becomes:

$$\Psi(\rho,\phi;\mathbf{r}) \approx 2nk\sin^2(\alpha/2)\left\{(x\rho\cos\phi + y\rho\sin\phi)\sqrt{\frac{1}{\sin^2(\alpha/2)} - \rho^2} + z\left(\frac{1}{2\sin^2(\alpha/2)} - \rho^2\right)\right\}, \tag{12}$$

where we notice that the defocus term is accurately described by a quadratic and so results in a perfect axial focus. Lateral displacements, however, result in a curved phase profile which cannot be focused stigmatically.

A particularly interesting property of the pupil function is the odd parity that it possesses which can be formally stated as:

$$\Psi(\rho,\phi;-\mathbf{r}) = -\Psi(\rho,\phi;\mathbf{r}). \tag{13}$$

This is simply the statement that a point source placed at $\mathbf{r}$ produces an equal and opposite phase distribution to a source placed at $-\mathbf{r}$ as can be seen in Fig. 3. This odd parity condition is the direct result of the form of Eq. (7) and is therefore applicable to the sine condition, Herschel condition and other transformations such as the uniform projection condition and Helmholtz condition.

Due to the reciprocal nature of ray optics we also note that if a wavefront could be generated at the pupil plane with the same form as that in Eq. (9) but traveling into the lens then there would be stigmatic convergence to a single point. Such wavefronts could be manufactured with a deformable mirror. However, a simpler method can be inferred by considering the situation in Fig. 3. If the orientation of the second lens were reversed and the pupil function from the first lens was imaged into the pupil plane of the second lens then the wavefront would be of exactly the right form to cause convergence to a single point.

This applies for all positions of the initial point source in three-dimensions so long as $r \ll f$ and is the direct consequence of the odd parity condition.

4. A technique for remote focusing

We now suggest a strategy that allows refocusing to be carried out without moving the object under examination. In essence, this strategy involves constructing a perfect imaging system which replicates the three-dimensional distribution of object space in the focal region of a second high NA objective lens with a magnification of n_1/n_2, as just described, and then uses a further microscope to image this replica. Refocusing is then carried out by moving the microscope with respect to the replica, which can be done without introducing any movements near the object itself.

The first stage is shown in Fig. 4 and comprises two objective lenses back-to-back with a 4f imaging stage mapping the pupil planes together. In general the objective lenses L1 and L2 need not be identical and may operate with different immersion media $-n_1$ and n_2 respectively. For the practical case of objectives obeying the sine condition, we can write down the phase profile generated in the pupil plane of this system for a point source located at the position (x,y,z) in the focal region of L1:

$$\Psi_1(\rho_1,\phi) = kn_1\sin\alpha\left(x\rho_1\cos\phi + y\rho_1\sin\phi + z\left(\frac{1}{\sin^2\alpha_1} - \rho_1^2\right)^{1/2}\right). \tag{14}$$

It is also possible to write down the phase profile required to focus all the rays stigmatically to a point located at $(n_1/n_2)\times(x,y,z)$ in the focal region of L2:

$$\Psi_2(\rho_2,\phi) = kn_2\sin\alpha_2\frac{n_1}{n_2} \times\left(x\rho_2\cos\phi + y\rho_2\sin\phi + z\left(\frac{1}{\sin^2\alpha_2} - \rho_2^2\right)^{1/2}\right), \tag{15}$$

where the coordinate system is defined in the diagram. If the 4f system mapping the pupil planes together has magnification:

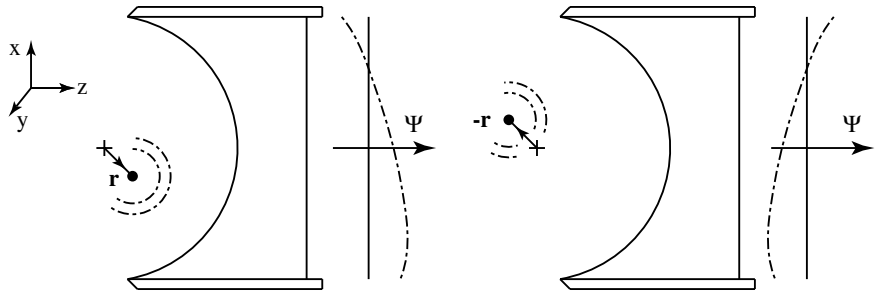

Fig. 3. Demonstration of odd parity pupil functions.

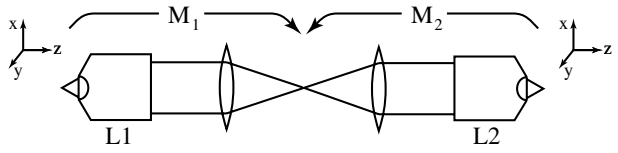

Fig. 4. Perfect imaging system.

$$M = \frac{\rho_2}{\rho_1} = \frac{\sin\alpha_1}{\sin\alpha_2} \tag{16}$$

then it can be seen that the two phase profiles identical and the point source is stigmatically imaged in the focal region of L2.

As a result the system images a three-dimensional region of object space with an isotropic magnification factor of n_1/n_2, consistent with the requirements of a perfect imaging system.

As a peripheral point we note that in some commercial microscopes the objectives are designed to work in conjunction with a specific tube lens whereby correction of certain aberrations is carried out by the two lenses working as a pair. Using objectives such as these in the current system would not therefore guarantee optimal performance. It is possible to avoid potential problems, however, by using objective lenses where the correction has been done internally instead.

The design of the perfect imaging system can also be understood by considering the system as two separate microscope systems back-to-back such that the first magnifies the object by a factor M_1 and the second demagnifies by M_2. In this situation both the lateral and axial magnifications of microscope combination yield the same value of n_1/n_2, as required for perfect imaging of the three-dimensional domain. In effect the spherical aberration introduced by the first system is directly compensated by that introduced by the second. Care must be taken, however, when constructing the system in this way to ensure that the tube lenses form a 4f imaging system linking the pupil planes correctly. Commercial microscopes often place the tube lens closer to the objective than is necessary here because this does not affect standard microscope operation. However, extra phase curvature introduced for axially displaced points in the current system would lead to a degradation of system performance.

We also note that rays from the object space are mapped onto conjugate rays with the same angle in image space, in accordance with Eq. (2). As such it is possible to see that the limiting angular aperture in the system γ_{max} will essentially limit the overall resolution of the instrument. The effective numerical aperture can therefore be evaluated by projecting this angle back into the object space to find $NA = n_1 \sin\gamma_{max}$. This implies that as long as the second objective has a higher *angular aperture* than the first it will not restrict the resolution, a situation that is easily realized when using say, a 1.4NA oil immersion lens and a 0.95NA dry lens as L1 and L2 respectively.

Having produced a three-dimensional replica of the object we now magnify and image planes of this using a third microscope system, which also comprises a high NA objective lens (L3) and tube lens, as shown in Fig. 5a. Refocusing is carried out by moving L3 axially so that different planes of the intermediate image space are imaged without spherical aberration. As a result, we have constructed a system where refocusing can be carried out remotely, without moving the original object and without introduction of spherical aberrations.

We also present a second system that enables superior axial scan speeds while refocusing. This is shown in Fig. 5b and is optically identical to the system already discussed. In this arrangement a plane mirror reflects the rays from the intermediate image space back into L2 and a beam splitter is further used to direct these towards the final tube lens and image plane. L2 is therefore used twice: once to cancel the aberrations introduced by L1 and once as part of the third microscope. By moving the mirror, it is possible to change which plane of the object is imaged perfectly at the image plane without spherical aberration. As the distribution in the intermediate image space has roughly the same dimensions as the object itself the mirror can be very small and can therefore be scanned quickly,

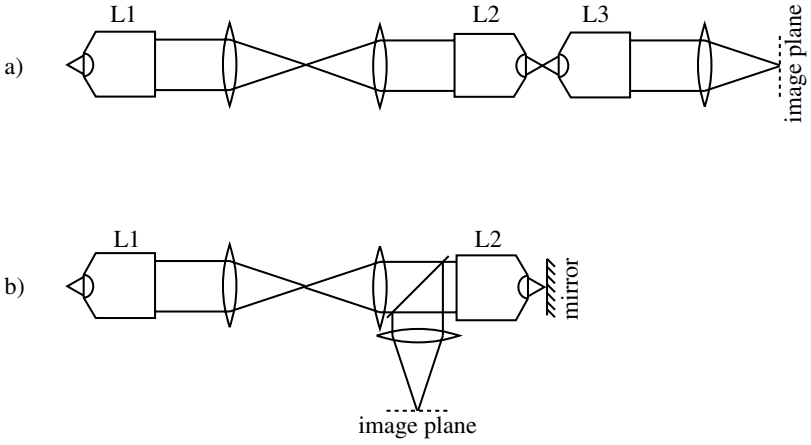

Fig. 5. Two systems comprising a perfect imaging system and a further microscope for magnification.

providing faster refocusing speeds than were possible by moving L3 in the previous arrangement.

5. Range of operation

We have so far only considered the lowest order contribution in the pupil phase of Eq. (6). This is a good approximation when considering small displacements from focus however a full description must incorporate the higher order terms of the expansion too. In this section we establish the range of operation for the cases where objective lenses obeying the sine condition are used.

Consider a system such as the one shown in Fig. 4 where the two objective lenses are identical and their pupil planes are mapped together with a 4f imaging system having unit magnification. In the first approximation we found that a point source located at a distance z along the axis from the focus of L1 forms a conjugate image point a distance z along the axis from the focus of L2. A general ray traveling between these two points crosses the pupil plane at position (ρ,ϕ) and carries a phase due to its relative path length during propagation. It is possible to find the total phase introduced for each ray traveling between conjugate points by summing the phase contributions introduced by each objective, as defined in Eq. (6):

$$\Delta\Psi = -nkf\left[\left\{1-\frac{2z}{f}(1-\rho^2\sin^2\alpha)^{1/2}+\frac{z^2}{f^2}\right\}^{1/2} + \left\{1+\frac{2z}{f}(1-\rho^2\sin^2\alpha)^{1/2}+\frac{z^2}{f^2}\right\}^{1/2}-2\right] \tag{17}$$

If the path length difference between the point source and conjugate image point is the same for all rays then stigmatic imaging follows, which equivalently requires this expression to be constant across the pupil plane. This is the case for small displacements, as the first order terms in the binomial expansion of each contribution cancel, forcing $\Delta\Psi$ to be zero across the pupil. For larger displacements, though, higher order terms in the expansion will have a contributory effect so different rays have a slightly different phases which results in a breakdown of stigmatic imaging. Expanding Eq. (17) to find the term in z^2 yields:

$$\Delta\Psi = -\frac{kn^2\rho^2\sin^2\alpha}{f}z^2, \tag{18}$$

A convenient parameter that can be used to quantify the breakdown in stigmatic imaging is the Strehl ratio. This can be defined as the ratio of the maximum intensity of the spot formed for a point source at z and a point source in focus. This can be evaluated directly from the phase profile in Eq. (17) and is given by the following expression [10]:

$$S = \left|\frac{1}{\pi}\int \exp(j\Delta\Psi)\rho\,\mathrm{d}\rho\,\mathrm{d}\phi\right|^2 \approx 1-\frac{1}{\pi}\int(\Delta\Psi)^2\rho\,\mathrm{d}\rho\,\mathrm{d}\phi, \tag{19}$$

where integration is over pupil plane and the approximation is valid for Strehl ratios down to a value of 0.8. Before calculating the Strehl ratio though, it is necessary to remove the contributions of piston and high NA defocus from $\Delta\Psi$, since these do not affect the shape of the focal spot or the maximum intensity. These modes have the form:

$$\Psi_\mathrm{p} = 1,$$
$$\Psi_\mathrm{d} = nk(1-\rho^2\sin^2\alpha)^{1/2} - \frac{2nk}{3\sin^2\alpha}(1-\cos^3\alpha) \tag{20}$$

where piston is associated with a constant phase offset across the pupil whereas defocus has a more complicated form which can be inferred from Eq. (9) as $[n(1-\rho^2\sin^2\alpha)^{1/2}]$ with a constant offset chosen to ensure that its average value over the pupil is zero. As a result, these modes are orthogonal and the coefficient of piston, a, adds a constant phase to all rays whereas the coefficient of defocus, which we denote as δz, can be interpreted as an additional axial shift of the final image point in the focal region of L2.

We first find the coefficients of piston, a, and defocus, δz contained in $\Delta\Psi$ using standard techniques:

$$a = \frac{\int\Delta\Psi\Psi_\mathrm{p}\rho\mathrm{d}\rho}{\int(\Psi_\mathrm{p})^2\rho\mathrm{d}\rho} = -\frac{nk\rho^2z^2\sin^2\alpha}{f},$$
$$\delta z = -\frac{\int\Delta\Psi\Psi_\mathrm{d}\rho\mathrm{d}\rho}{\int(\Psi_\mathrm{d})^2\rho\mathrm{d}\rho} = -\frac{12z^2\cos^2\left(\frac{\alpha}{2}\right)(3+6\cos\alpha+\cos2\alpha)}{5f(3+8\cos\alpha+\cos2\alpha)} \tag{21}$$

and then use these to redefine a new aberration function:

$$\Delta\Psi' = \Delta\Psi - a\Psi_\mathrm{p} - \delta z\Psi_\mathrm{d} \tag{22}$$

which we insert into Eq. (19) to find the Strehl ratio. This can be done analytically and after some routine but rather protracted calculations a simple result emerges:

$$S = 1-\frac{4n^2k^2z^4(3+16\cos\alpha+\cos2\alpha)\sin^8\left(\frac{\alpha}{2}\right)}{75f^2(3+8\cos\alpha+\cos2\alpha)} \tag{23}$$

This function is plotted in Fig. 6a for the case of a 60× 1.4NA oil immersion objective, which has a value of $f = 4.55$ mm, and for a wavelength of 633 nm. We see from this that the Strehl ratio is greater than 0.8 for up to ±70 μm of point source displacement. Also plotted in Fig. 6b is the coefficient of defocus, δz, for different point source positions. This plot shows us that the image point will be slightly displaced along the axis compared with the prediction of the first order theory. Both these functions are even in z and are therefore symmetric about the origin.

As a final comment we point out that further extension of the range over which the system will operate can be realized if these residual aberrations where further corrected for by a deformable mirror although this would increase the complexity of the system.

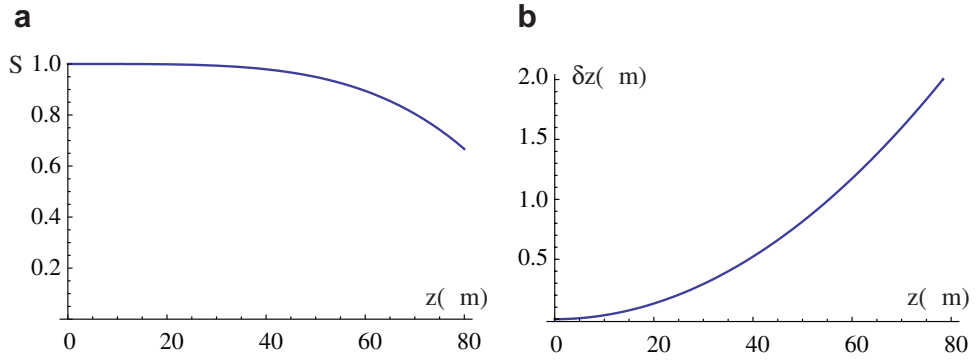

Fig. 6. (a) The Strehl ratio and (b) the coefficient of defocus as a function of point source position for the system shown in Fig. 4.

6. Point spread function measurements

A common way to characterize the performance properties of a microscope imaging system is to measure the system point spread function (PSF). There are many methods to do this and a particularly simple one, which is appropriate for our purposes, is based on a method for measuring the optical sectioning strength of a confocal microscope, see p. 103 of [11]. If a plane reflector is moved axially through the focal region of an objective lens the signal detected through a confocal pinhole is given by $|h(2z, r_d)|^2$ where $h(z, r)$ is the amplitude PSF, z denotes the displacement of the mirror from focus and r_d is the radial distance in the detector plane. A CCD camera can be treated as an array of pinholes, provided that the pixel sizes are small enough and it is therefore possible to measure entire planes of the PSF in a single frame. The axial position of the CCD camera defines the position of the nominal focal plane about which the PSF is measured.

We began by measuring the PSF of a microscope objective that obeys the sine condition to illustrate how spherical aberration is introduced when trying to refocus to different depths in the sample by moving the detector axially. We used the confocal configuration shown in Fig. 7a with the CCD camera acting as an effective pinhole array. An expanded beam from a helium neon laser (wavelength 633 nm) was coupled into the pupil of objective lens L1 using a beam splitter. An object mirror (M1) placed a distance z from the focal plane reflected the beam back through L1 and through the tube lens, which focussed the beam onto a CCD camera. L1 was an Olympus 1.4NA 60× oil immersion objective where all aberrations are corrected for internally; the tube lens was an achromatic doublet with focal length 160 mm. The axial position Z_C of the CCD camera could be changed in order to probe different parts of the object space. For each position of the CCD camera, a sequence of images was acquired for a range of z values. This image stack represents a three-dimensional intensity distribution which is mathematically identical to the intensity PSF for detection when imaging in the plane at Z_C. Fig. 8a shows the measured PSFs for five different positions of the CCD camera (Z_C(mm) $= -20, -10, 0, 10, 20$). All PSFs are presented on the same plot showing the meridional plane in object space. Three of the PSFs have been enlarged so that the distortions due to spherical aberration can be seen more clearly. As can

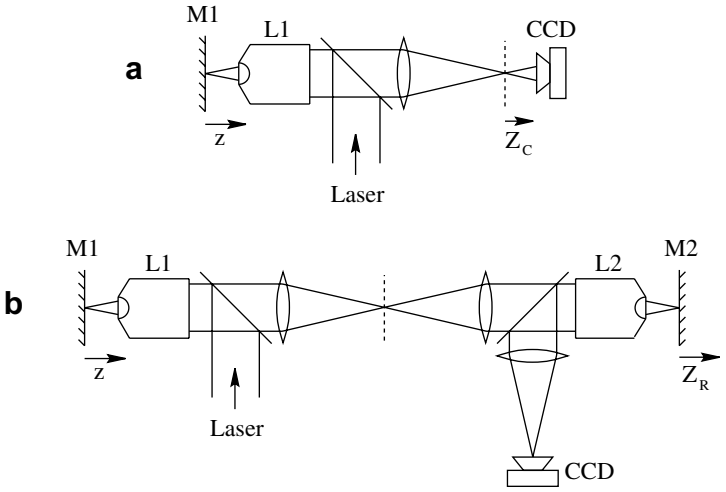

Fig. 7. Systems used to measure detection PSFs where z is the axial coordinate in the focal region of objective lens L1.

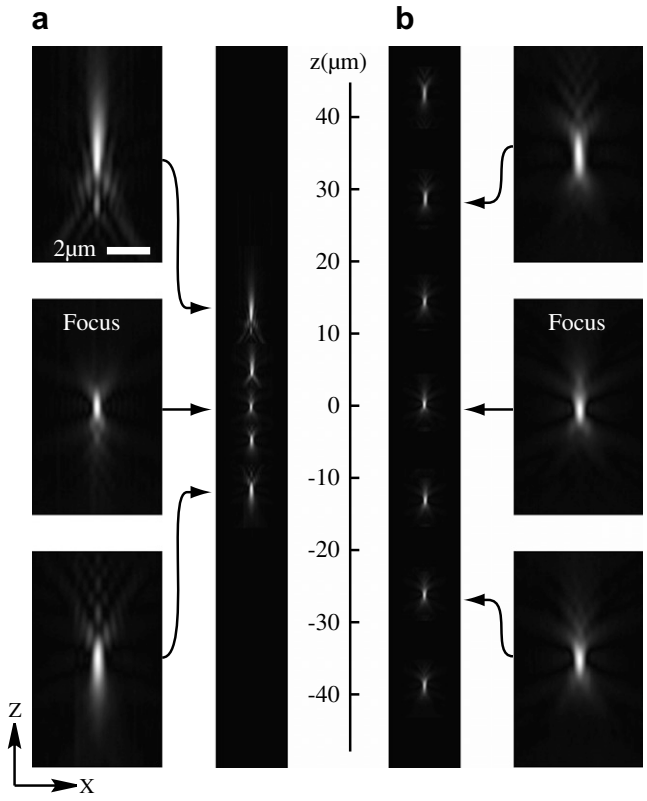

Fig. 8. Detection PSFs measured with the systems in Fig. 7.

be seen there is an elongation of the PSF along the axial direction. The intensity for each PSF has been re-normalized to the maximum pixel value in order that the images can be seen clearly.

The second set of measurements were made using the configuration of Fig. 7b. M1 was illuminated in the same way as before and the reflected light passed back through L1 and the first tube lens before passing through a second identical tube lens. The light then entered objective L2, which was an Olympus 0.95NA 40× dry objective. A dry lens was chosen to ensure that there was no mechanical interference between the reference mirror and the objective via an immersion medium. The light reflected off the reference mirror positioned at Z_R, re-entered L2 and was reflected by the beam splitter. Another tube lens focussed the light onto the CCD camera which was fixed in the nominal focal plane of the final microscope stage. For each position Z_R of the reference mirror, a sequence of images was acquired for a range of object mirror positions z and once again the resulting image stack can be shown to be equivalent to the intensity PSF for detection. Fig. 8b shows the measured PSFs for seven different positions of the reference mirror $(Z_R(\mu m) = -30,\ -20,\ -10, 0, 10, 20, 30)$. It can be seen that the overall shape of the PSF was retained over a large range of depths in object space, indicating that no significant aberrations were introduced. This can be seen clearly in the three PSFs that have been enlarged. Note that no intensity renormalization was performed for these three images. We also measured the Strehl intensity for each of the focal spots and found this to be roughly constant over a range of ±35 μm in object space.

7. Conclusions

In this paper we have presented a optical system for high NA imaging systems that allows optical refocusing to be performed without introducing significant spherical aberration. In essence, a single microscope system, obeying the sine condition, is replaced by a combination of three such systems. The system can be further refined by using a small reference mirror that replaces the third objective lens. We anticipate that this will be useful for three main reasons: firstly, this method allows faster axial scan rates than are currently available and hence XZ scanning or indeed scanning along arbitrary trajectories at high speed becomes possible. Secondly the specimen remains stationary and hence is not disturbed by the refocusing. Thirdly, this method permits extension of the working distance of the objective. The system is expected to be particularly useful for in vivo and non-invasive imaging applications.

Acknowledgements

E. Botcherby was supported by a MRC/DoH Clinician Training Fellowship. M. Booth is a Royal Academy of Engineering/EPSRC Research Fellow and R. Juškaitis was supported by RCUK/BBSRC.

References

[1] T. Wilson, C.J.R. Sheppard, Theory and practice of Scanning Optical Microscopy, Academic Press, London, 1984.
[2] W. Göbel, B.M. Kampa, F. Helmchen, Nature Meth. 4 (1) (2007) 73.
[3] N. Callamaras, I. Parker, Cell Calcium 26 (1999) 271279.
[4] H. Oku, K. Hashimoto, M. Ishikawa, Opt. Express 12 (2004) 2138.
[5] B. Qi, A. Phillip Himmerb, L. Maggie Gordonc, X.D. Victor Yangc, L. David Dickensheets, I. Alex Vitkina, Opt. Comm. 232 (2004) 123.
[6] G.D. Reddy, P. Saggau, J. Biomed. Opt. 10 (2005) 064038.
[7] E. Botcherby, R. Juškaitis, M. Booth, T. Wilson, Opt. Lett. 32 (14) (2007) 2007.
[8] J.C. Maxwell, Quart. J. Pure Appl. Maths. 2 (1858) 233.
[9] Max Born, Emil Wolf, Principles of Optics, sixth ed., Pergamon Press, 1983.
[10] V.N. Mahajan, Optical Imaging and AberrationsPart II. Wave Diffraction Optics., SPIE, Bellingham, Wash, 2001.
[11] T. Wilson, Confocal Microscopy, Academic Press, 1990.